

*Anthropogenic impacts on changes in summer extreme precipitation over China during 1961–2014: roles of greenhouse gases and anthropogenic aerosols*

Article

Accepted Version

Guo, Y., Dong, B. ORCID: <https://orcid.org/0000-0003-0809-7911> and Zhu, J. (2023) Anthropogenic impacts on changes in summer extreme precipitation over China during 1961–2014: roles of greenhouse gases and anthropogenic aerosols. *Climate Dynamics*, 60. pp. 2633-2646. ISSN 0930-7575 doi: <https://doi.org/10.1007/s00382-022-06453-4> Available at <https://centaur.reading.ac.uk/106956/>

It is advisable to refer to the publisher's version if you intend to cite from the work. See [Guidance on citing](#).

To link to this article DOI: <http://dx.doi.org/10.1007/s00382-022-06453-4>

Publisher: Springer

All outputs in CentAUR are protected by Intellectual Property Rights law, including copyright law. Copyright and IPR is retained by the creators or other copyright holders. Terms and conditions for use of this material are defined in the [End User Agreement](#).

[www.reading.ac.uk/centaur](http://www.reading.ac.uk/centaur)

**CentAUR**

Central Archive at the University of Reading

Reading's research outputs online

1 **Anthropogenic impacts on changes in summer extreme precipitation**  
2 **over China during 1961-2014: roles of greenhouse gases and**  
3 **anthropogenic aerosols**

4  
5  
6  
7  
8  
9 **Yan Guo<sup>1\*</sup>, Buwen Dong<sup>2</sup>, Jiangshan Zhu<sup>3</sup>**

- 10  
11  
12  
13 *1. State Key Laboratory of Earth Surface Processes and Resource Ecology, Beijing*  
14 *Normal University, Beijing 100875, China*  
15 *2. National Centre for Atmospheric Science, Department of Meteorology,*  
16 *University of Reading, Reading, UK*  
17 *3. Institute of Atmospheric Physics, Chinese Academy of Sciences, Beijing 100029,*  
18 *China*

19  
20  
21  
22  
23  
24  
25  
26  
27  
28  
29  
30  
31  
32  
33  
34  
35  
36  
37  
38  
39 \*Corresponding author: Yan Guo ([guoyan@bnu.edu.cn](mailto:guoyan@bnu.edu.cn))  
40

41 **Abstract**

42 Extreme precipitation often causes enormous economic losses and severe disasters.  
43 Changes in extreme precipitation potentially have large impacts on the human society.  
44 In this study, we investigated the changes in four precipitation extreme indices over  
45 China during 1961~2014. The indices include total wet-day precipitation (PRCPTOT),  
46 precipitation on extremely wet days (R95pTOT), number of extremely wet days (R95d)  
47 and precipitation intensity on extremely wet days (R95int) during the extended summer  
48 (May-August). Observation analyses showed that these four indices have significantly  
49 increased over southeast China (SEC) and northwest China (NWC) whilst decreased  
50 over northeast China (NEC) and southwest China (SWC). Based on HadGEM3-GC3.1  
51 historical, greenhouse gas only (GHG) and anthropogenic aerosol only (AA)  
52 simulations, we assessed the relative roles of different forcings in the observed trends.  
53 Model reproduced the main features of increasing trends over SEC and NWC in  
54 historical simulations, suggesting a dominant role of forced changes in the trends of  
55 four indices over the two regions. Individual forcing simulations indicated that GHG  
56 and AA forcings influence the increases in summer extreme precipitation over SEC and  
57 NWC, respectively, through different processes. Over SEC, extreme precipitation  
58 increase is mainly due to GHG forcing that results in moisture flux convergence  
59 increase through thermodynamic and dynamic effects. In comparison to GHG forcing,  
60 AA forcing has a weak contribution because AA forced moisture flux convergence  
61 increase is offset by AA forced evaporation reduction. Over NWC, extreme  
62 precipitation increase is primarily attributed to AA forcing and secondarily to GHG  
63 forcing. AA forcing can result in moisture flux convergence increase through dynamic  
64 effect, and GHG forcing can result in evaporation increase.

65 **Key words** summer extreme precipitation, anthropogenic impact, greenhouse gases,  
66 aerosols, China

67

## 68 **1. Introduction**

69 Increased frequency and intensity of extreme precipitation have been observed in  
70 the context of global warming, which have prominent impacts on the human society,  
71 ecosystems, and environment (IPCC, 2021). Extreme precipitation often causes  
72 enormous economic losses and severe disasters. East China has experienced significant  
73 increases in extreme precipitation during the last few decades (Zhou et al. 2016), which  
74 cause enormous economic losses due to locally high population density and rapid  
75 economic development. For example, the annual economic losses caused by floods  
76 increased from 80.2 billion Yuan during 1984~2003 to 122.83 billion Yuan during  
77 2004~2013 over China (Qin et al., 2015). Therefore, understanding the causes for  
78 changes in extreme precipitation over China and providing reliable projection of future  
79 changes are of great significance, which are particularly concerned by both scientific  
80 community and decision makers.

81 Human-induced increases in greenhouse gases (GHGs) have contributed to the  
82 observed intensification of extreme precipitation over many land areas (Min et al. 2011;  
83 Zhang et al. 2013, Dong et al. 2020, 2021). GHG impacts have been detected over  
84 China both on the increasing trend of precipitation extremes (Chen and Sun 2017; Li et  
85 al. 2017; Lu et al. 2020) and individual heaviest precipitation events (Sun et al. 2019).  
86 Physically, GHG induced global warming could enhance atmospheric water holding  
87 capacity, favoring more heavy precipitation. Meanwhile, GHG induced modulation of  
88 the East Asian summer monsoon (EASM) circulation can give rise to more moisture  
89 flux convergence over east China, favorable to more heavy precipitation (Ma et al.  
90 2017). It was demonstrated that under GHG forcing, EASM circulation can be  
91 modulated through intensified land-ocean thermal contrast as well as uneven warming  
92 of sea surface temperature (SST) that resulted in intensified western North Pacific  
93 subtropical high (WNPSH) via strengthened local Hadley circulation (Tian et al. 2018)  
94 or weakened Walker circulation (Lin et al. 2020).

95 In addition to GHGs, increases in anthropogenic aerosol (AA) emissions have  
96 essential influences on precipitation changes, although its influences are complex that  
97 includes direct (aerosol radiation interaction) and indirect impacts (aerosol cloud  
98 interaction). By scattering and absorbing solar radiation, aerosols can prevent the  
99 shortwave radiation reaching the earth surface, termed as aerosol radiation interaction.  
100 By directly interacting with cloud, aerosols can change cloud radiation properties and

101 precipitation efficiency, termed as aerosol cloud interaction (Dong et al. 2019). Besides  
102 direct interaction with cloud through microphysical processes to affect precipitation,  
103 aerosols have the potential to affect circulation through altering radiation budget. AAs  
104 have been demonstrated to play an important role for the observed weakening of the  
105 EASM circulation (Dong et al. 2019; Song et al. 2014; Tian et al. 2018) and the reduced  
106 summer extreme precipitation over north China (Lin et al. 2018; Zhang et al. 2017). Ma  
107 et al. (2017) showed evidences that AA could partially offset the GHG induced  
108 increases in heavy precipitation over east China.

109 Although previous studies have investigated the anthropogenic influences on  
110 precipitation changes over China, a few studies focused on the changes in extreme  
111 precipitation defined by percentile-based extreme indices, and the exact physical  
112 mechanism underlying are still not clear. In this study, our main aim is to elucidate the  
113 relative roles of GHG forcing and AA forcing on the changes in summer extreme  
114 precipitation over China, and to understand the physical processes responsible. We use  
115 a set of experiments based on a state-of-the-art climate model HadGEM3 in the Global  
116 Coupled configure (HadGEM3-GC3.1) that participates in the sixth phase of Coupled  
117 Model Inter-comparison Project (CMIP6) (e.g., Eyring et al., 2016; Gillett et al., 2016)  
118 to address these above questions.

119 The structure of this paper is designed as follows: Sect.2 introduces the  
120 observational data, model and methodology. Sect.3 illustrates the observed changes in  
121 summer precipitation extremes over China. Sect.4 elucidates the anthropogenic roles  
122 including GHG forcing and AA forcing in shaping these changes and analyzes the  
123 related physical processes. Sect.5 and Sect.6 reveal the detailed physical mechanism in  
124 response to GHG forcing and AA forcing, respectively. Finally, our conclusion and  
125 discussion are summarized in Sect.7.

## 126 **2. Observational data, model and methodology**

127 As a reference from observation, gridded daily precipitation data with a spatial  
128 resolution of  $1^\circ \times 1^\circ$  since 1961 were obtained from the CN05.1 dataset (Wu and Gao  
129 2013). The CN05.1 dataset is produced by the National Climate Centre of the China  
130 Meteorological Administration from more than 2400 observational stations covering  
131 all of mainland China. The reliability of this dataset has been widely confirmed by  
132 previous research focused on climate over China (Luo et al., 2021; Zhou et al. 2016).

133 HadGEM3-GC3.1 represents the UK's contribution to the CMIP6 (e.g., Andrews

134 et al., 2020). This physical climate model consists of global atmosphere-land  
135 configuration GA7/GL7.1, the global ocean GO6 and the sea ice model configuration  
136 GSI8.1, coupled with the OASIS-MCT coupler. Its lower resolution configuration was  
137 used in this study, which has a nominal atmospheric resolution of 135 km (85 levels)  
138 and an ocean resolution of 1° (75 levels) with coupling every 3 hours. Three types of  
139 experiment designed in CMIP6 were employed, which are (1) historical simulations  
140 with all external forcings (All) including external anthropogenic forcings (GHGs, AAs,  
141 ozone, and land use) and external natural forcings (solar and volcanic activities); (2)  
142 GHG-only simulations (GHG) forced by GHGs only; (3) AA-only simulations (AA)  
143 forced by AAs only (e.g., Eyring et al., 2016; Gillett et al., 2016). A common period  
144 1961~2014 among three experiments were concerned. All five ensemble members  
145 r1i1p1f3~r5i1p1f3 were used. Ensemble mean of five ensemble members was used to  
146 represent the external forced responses.

147 Changes of extreme precipitation during the boreal extended summer from May  
148 to August were studied. Four precipitation extreme indices were used which are defined  
149 according to the approach recommended by the Expert Team on Climate Change  
150 Detection and Indices (ETCCDI), i.e., total wet-day precipitation (PRCPTOT, unit:  
151 mm), precipitation on extremely wet days (R95pTOT, unit: mm), number of extremely  
152 wet days (R95d, unit: days), precipitation intensity on extremely wet days (R95int, unit:  
153 mm/day). A wet day was defined as daily precipitation  $\geq 1$  mm. An extremely wet day  
154 was defined as daily precipitation  $>$  the 95<sup>th</sup> percentile of daily precipitation on wet  
155 days over the base period 1961~1990 in the boreal extended summer. We used linear  
156 trend to describe the long-term change, which is estimated using the least square  
157 method and its statistical significance is tested using a two-tailed Student's t-test.

### 158 **3. Observed changes in summer precipitation extremes**

159 Figure 1 shows the observed trends of summer wet-day total amount (PRCPTOT),  
160 extremely wet-day amount (R95pTOT), extremely wet-day frequency (R95d), and  
161 extremely wet-day intensity (R95int) during 1961~2014 (54 years as 54a). Changes in  
162 PRCPTOT, R95pTOT, and R95int are expressed as percentage relative to the  
163 climatology over 1961~1990. Patterns of trends in these four extreme indices show a  
164 common feature, which is increase over the southeast and northwest China whilst  
165 decrease over the northeast and southwest China. Changes in both extreme precipitation  
166 frequency and intensity are in agreement with extreme precipitation amount, suggesting

167 that more extreme precipitation events occur over the southeast and northwest China  
168 with strengthened intensity, and oppositely less extreme precipitation events occur over  
169 the northeast and southwest China with weakened intensity.

170 To facilitate quantitative depiction, whole China was divided into four sub-regions,  
171 i.e., southeast China (SEC), northeast China (NEC), northwest China (NWC), and  
172 southwest China (SWC) as shown in Fig.1. The trends of regional averaged extreme  
173 indices were calculated over these four regions and shown in Fig.2 (white bar). Over  
174 SEC, PRCPTOT has increased at 8.8%/54a and R95pTOT has increased at 25%/54a.  
175 Responsible for the R95pTOT increase, R95d and R95int have consistently risen with  
176 rates of 0.7 days/54a and 7.4%/54a respectively. Similarly, significantly increasing  
177 trends are seen over NWC in the four extreme indices, which are 15.4%/54a in  
178 PRCPTOT, 34%/54a in R95pTOT, 0.8 days/54a in R95d, and 15.1%/54a in R95int.  
179 Contrary to the increases of precipitation extremes over SEC and NWC, precipitation  
180 extremes decreases are observed over NEC and SWC, not significant though.

#### 181 **4. Model simulated changes in precipitation extremes and related processes in** 182 **response to different forcings**

183 To understand the underlying drivers for the observed changes in precipitation  
184 extremes and the physical mechanism involved, a set of simulations based on  
185 HadGEM3-GC3.1 were analyzed. Figure 3a-3d are the simulated trends of four extreme  
186 indices in response to All forcing. Overall, model is able to reproduce precipitation  
187 extremes increases over SEC and NWC. This is consistent among five ensemble  
188 members. The simulated trends over SEC are  $22.7 \pm 6.7\%/54a$  in R95pTOT,  $0.5 \pm 0.16$   
189 days/54a in R95d, and  $6.4 \pm 2.9\%/54a$  in R95int (blue bars in Fig.2), being very close to  
190 observation. The simulated trends over NWC are  $15.1 \pm 6.4\%/54a$  in R95pTOT,  $0.3 \pm$   
191  $0.17$  days/54a in R95d, and  $7.6 \pm 5.6\%/54a$  in R95int (blue bars in Fig.2), being  
192 underestimated to some extent but still significant. Above results suggest a dominant  
193 role of forced changes in the recent trends of extreme indices over the two regions.  
194 Observed decreases of precipitation extremes over NEC and SWC are not reproduced  
195 by model ensemble mean, as demonstrated by opposite trends against observation. The  
196 associated possible reasons will be discussed later. In the following, we will explore  
197 the detailed processes associated with the changes in summer precipitation extremes

198 just over SEC and NWC, rather than over all China, based on model HadGEM3-GC3.1.

199 To explore the anthropogenic effects on the changes in summer precipitation  
200 extremes over SEC and NWC, the simulated trends in four extreme indices in response  
201 to GHG forcing and AA forcing are respectively shown in Fig.3e-3h and Fig.3i-3l.  
202 GHG forced pattern, resembling that in response to All forcing, is characterized by  
203 prominent increases over the Yangtze-Huai River Basin and northwest China. AA  
204 forced pattern shows a meridional dipole feature characterized by decrease over the  
205 Yangtze River as well as its southern region and increase over northern China.

206 Trends of regional averaged extreme indices over SEC and NWC in response to  
207 individual GHG forcing and AA forcing are shown in Fig. 2 (gray and green bars). Over  
208 SEC, prominent increase of precipitation extremes are provided in response to GHG  
209 forcing with trends of  $29.9\pm 6\%/54a$  in R95pTOT,  $0.9\pm 0.26$  days/54a in R95d, and  $8.6$   
210  $\pm 3.8\%/54a$  in R95int, being consistent with those in response to All forcing. In contrast,  
211 decrease of precipitation extremes are provided in response to AA forcing with trends  
212 of  $-3.4\pm 12.8\%/54a$  in R95pTOT,  $-0.07\pm 0.38$  days/54a in R95d, and  $-3.8\pm 2.7\%/54a$  in  
213 R95int. These results imply that model simulated increase of summer precipitation  
214 extremes over SEC is predominantly due to GHG forcing, rather than AA forcing.  
215 Unlike over SEC, model provided increased precipitation extremes over NWC in  
216 response to both GHG forcing and AA forcing with trends of  $11.5\pm 4.8\%/54a$  and  $6.1\pm$   
217  $8\%/54a$  in R95pTOT,  $0.2\pm 0.05$  days/54a and  $0.13\pm 0.13$  days/54a in R95d, and  $3.8\pm$   
218  $3.7\%/54a$  and  $4.9\pm 4.8\%/54a$  in R95int, indicating that model simulated increase of  
219 summer precipitation extremes over NWC is due to both GHG forcing and AA forcing.

220 As we know that global warming increases the water holding capacity of the  
221 atmosphere, thus mean precipitation is expected to increase, and precipitation  
222 characteristics are expected to change. A significant shift in probability distribution  
223 functions (PDFs) of tropical precipitation toward intense rain have been expected  
224 (Trenberth et al. 2003) and also widely observed (Lau et al. 2007). Ma et al. (2017) also  
225 indicated this shift in PDFs of summer precipitation over East China. Increased mean  
226 precipitation is contributed by increased extreme precipitation, suggesting an  
227 association of increases between the mean precipitation and extreme precipitation,

228 although their increasing rate are different. In our study, changes in mean precipitation  
229 and precipitation extremes are in agreement with each other. As Fig.1 shows, the pattern  
230 of trend in PRCPTOT resembles those in R95pTOT, R95d and R95int with pattern  
231 correlation coefficients of 0.76, 0.54 and 0.6, respectively. And these associations are  
232 well represented in model. The pattern correlation coefficients of trend in PRCPTOT  
233 with that in R95pTOT, R95d and R95int are 0.84, 0.71, and 0.62 respectively in  
234 historical simulation. Mean precipitation increase usually exhibits extreme  
235 precipitation increase, therefore understanding the mechanisms responsible for mean  
236 precipitation increase will help us to understand that for extreme precipitation increase.

237 To investigate what processes contribute to the increases of summer precipitation  
238 over SEC and NWC, atmospheric moisture budgets have been examined. According to  
239 moisture budget equation, precipitation is balanced by evaporation and vertically  
240 integrated atmospheric moisture flux convergence at monthly or longer time scale  
241 (Trenberth and Guillemot 1995). Furthermore, the moisture flux convergence is  
242 decomposed into the dynamic component due to circulation changes and the  
243 thermodynamic component due to specific humidity changes, to facilitate studying the  
244 dynamic and thermodynamic effects (Li et al. 2015).

245 Figure 4 is the spatial pattern of trend in summer precipitation, evaporation,  
246 moisture flux convergence, and thermodynamic and dynamic components of moisture  
247 flux convergence in response to All forcing, GHG forcing, and AA forcing, respectively.  
248 Changes in precipitation (Fig. 4a-4c), evaporation (Fig. 4d-4f), and moisture flux  
249 convergence (Fig. 4g-4i) are compared. The similarity between changes in precipitation  
250 and moisture flux convergence indicates that moisture flux convergence change is  
251 predominantly responsible for precipitation change. Furthermore, the moisture flux  
252 convergence is decomposed into thermodynamic component (Fig. 4j-4l) and dynamic  
253 component (Fig. 4m-4o). The decomposition manifests that the pattern and magnitude  
254 of moisture flux convergence changes are mainly due to dynamic effect. Over SEC,  
255 thermodynamic effect also plays a role in response to All forcing (Fig. 4j) or GHG  
256 forcing (Fig. 4k), however it weakens dynamic effect in response to AA forcing (Fig.  
257 4l).

258 To quantify the impacts of different forcings on extreme precipitation changes  
259 over SEC and NWC via distinctive physical processes, the trends of regional averaged  
260 summer precipitation, evaporation, moisture flux convergence, thermodynamic and

261 dynamic components over SEC and NWC are respectively shown in Fig. 5. Over SEC,  
262 summer precipitation increase in response to All forcing (blue bar) is attributed to  
263 moisture flux convergence increase that is further caused by both dynamic (62%) and  
264 thermodynamic (46%) effects. Isolating the roles of GHG forcing and AA forcing  
265 demonstrates that precipitation increase over SEC is due to GHG forcing (gray bar).  
266 The GHG forced precipitation increase is dominated by moisture flux convergence  
267 increase (95%) that is further caused by both thermodynamic (48%) and dynamic (49%)  
268 effects. Differently, AA forced (green bar) moisture flux convergence increase is offset  
269 by evaporation reduction. Moreover, moisture flux convergence increase is due to  
270 dynamic effect (148%), rather than thermodynamic effect that contributes negatively  
271 (-46%).

272 Over NWC, summer precipitation increase in response to All forcing (blue bar) is  
273 attributed to increases in both evaporation (61%) and moisture flux convergence (72%).  
274 The increase in moisture flux convergence is due to dynamic effect (158%). Isolating  
275 the roles of GHG forcing and AA forcing demonstrates that precipitation increase over  
276 NWC is primarily attributed to AA forcing (green bar), and secondarily to GHG forcing  
277 (gray bar). AA forced precipitation increase is dominated by the moisture flux  
278 convergence increase (83%) that is mainly caused by dynamic effect (144%), while  
279 GHG forced precipitation increase is mainly from evaporation increase (100%).

## 280 **5. Mechanism related to GHG forcing**

281 As shown in Sect. 4, model simulated summer precipitation increase over SEC is  
282 resulted from moisture flux convergence increase that is caused by both thermodynamic  
283 effect due to humidity increase and dynamic effect owing to strengthened circulation  
284 convergence. What detailed processes are responsible for the changes in humidity and  
285 circulation?

286 As air temperature increases in response to rising GHG concentration,  
287 atmosphere can hold more moisture, as demonstrated by increased vertically integrated  
288 precipitable water over SEC (Fig. 6a), which favors precipitation increase. Additionally,  
289 in response to GHG forcing, the enhanced WNPSH leads to anomalous southwesterly  
290 winds prevailing over SEC (Fig. 6b) that transport more moisture from the Bay of  
291 Bengal and the South China Sea and converge over the Yangtze-Huai River Basin (Fig.  
292 4h), giving rise to local precipitation increase. These results basically agree with the  
293 results based on a specific model (MetUM-GOML2) with experiment design in

294 previous studies (Lin et al. 2020; Luo et al. 2019; Tian et al. 2018).

295 How does the WNPSH strengthen in response to GHG forcing? GHG forced SST  
296 changes show an El Nino-like SSTA (Fig. 6c), which is formed because the mixed layer  
297 depth is deeper over the western tropical Pacific than the eastern tropical Pacific, in  
298 turn, GHG forced warming is weaker over the west than the east. This mechanism has  
299 been indicated in the previous research (Collins et al. 2010). The zonal asymmetry of  
300 SST increase could weaken the Walker circulation (Fig. 6d), resulting in anomalous  
301 descent over the northwest Pacific and the enhanced WNPSH.

302 As indicated in Sect.4, GHG forced summer precipitation increase over NWC is  
303 mainly due to evaporation increase. What detailed process is responsible for the  
304 evaporation increase? Peng and Zhou (2017) investigated the summer precipitation  
305 increase over northwest China with reanalysis data, and they indicated that more than  
306 50% of the increase is balanced by evaporation increase. The increased evaporation is  
307 favored by increased net surface radiation that is largely originated from the increased  
308 clear sky downward longwave radiation. According to their conclusion, the change in  
309 clear sky surface downward longwave radiation under GHG forcing is examined (Fig.  
310 6e). Responding to GHG forcing, clear sky downward longwave radiation increases  
311 over all China, especially over northwest China and east China, which is responsible  
312 for the evaporation increase over there.

## 313 **6. Mechanism related to AA forcing**

314 As indicated in Sect.4, summer precipitation has not significantly changed over  
315 SEC in response to AA forcing, because the moisture flux convergence increase is  
316 offset by the evaporation reduction. Unlike over SEC, AA forced precipitation increases  
317 over NWC. It is resulted from moisture flux convergence increase, which is caused by  
318 dynamic effect due to strengthened circulation convergence. Detailed processes  
319 responsible for these changes are investigated in the following.

320 As indicated in previous research (Peng and Zhou 2017) that evaporation change  
321 is highly associated with net surface radiation change over NWC under GHG forcing,  
322 this association is demonstrated to exist over SEC in response to AA forcing (with  
323 correlation coefficient  $> 0.8$ ). As AA emission increases over SEC, the downward  
324 shortwave radiation will reduce owing to aerosol radiation interaction and aerosol cloud  
325 interaction, which leads to net surface radiation reduction (Fig.7a) and finally  
326 evaporation reduction over SEC. Additionally, as air temperature drops due to AA

327 radiation effect, atmospheric capability to hold moisture will weaken, as demonstrated  
328 by reduced vertically integrated precipitable water (Fig.7b), which is also unfavorable  
329 for the precipitation over SEC.

330 Considering the anomalous circulation in response to AA forcing, the strengthened  
331 WNPSH results in anomalous southwesterly winds transporting moisture from the  
332 South China Sea to the SEC. These anomalous southwesterlies further flow  
333 northwestward after crossing the Huai River and converge over the NWC (Fig. 7c).  
334 These anomalous circulations cause moisture flux convergence increase over both the  
335 Yangtze-Huai River Basin and eastern part of NWC (Fig.4i), favorable for local  
336 precipitation increase.

337 Firstly, what drives those anomalous circulations? In AA forcing experiment, two  
338 high-value centers of sea level pressure anomaly (SLPA) are formed over north China  
339 and north India, respectively (Fig. 7c), which agree with local cooling anomalies (Fig.  
340 7d) as AAs increase over there. In contrast, AAs are relatively low over the NWC,  
341 leading to relatively high air temperature anomaly (Fig. 7d) and relatively weak SLPA  
342 locally (Fig.7c). This spatial pattern of SLPA and associated zonal SLPA gradient  
343 between north China and NWC can lead anomalous southwesterlies to turn  
344 northwestward and become anomalous easterlies.

345 Secondly, how does the WNPSH strengthen in response to AA forcing? In Fig.7e  
346 (meridional section zonally averaged over  $105^{\circ}\text{E}\sim 145^{\circ}\text{E}$ ), anomalous descent is found  
347 at about  $20^{\circ}\text{N}$ , which is responsible for the WNPSH strengthening, whilst its north ( $30^{\circ}$   
348  $\text{N}\sim 40^{\circ}\text{N}$ ) and south ( $0\sim 10^{\circ}\text{N}$ ) sides are anomalous ascents. How does this anomalous  
349 meridional cell form over the northwest Pacific (NWP)? AA forced SST shows a tilted  
350 SSTA tripole pattern oriented in northwest-southeast direction lasting from the  
351 preceding winter to summer (Fig.8) with negative SSTA at about  $20^{\circ}\text{N}$  and positive  
352 SSTA on both northwest and southeast sides. This tilted SSTA tripole pattern and  
353 associated meridional SST gradient in pre-summer are responsible for the anomalous  
354 meridional cell shown in Fig.7e. This result is similar to the Fig.9 in Lin et al. (2020).  
355 As Lin et al. (2020) indicated, the anomalous cooling at about  $20^{\circ}\text{N}$  over NWP in pre-  
356 summer is highly associated with AA emissions that are advected from the East Asian  
357 continent by the prevailing winds.

358 To further understand why the meridional SSTA gradient disappears in the late  
359 summer (Fig.8d), we analyze the temporal evolution of zonally averaged (105°E~ 145°  
360 E) changes of SST, precipitation, total cloud amount and surface downward shortwave  
361 radiation related with cloud (Fig. 9). In Fig.9a, cooling SSTA at about 20°N is found to  
362 last from preceding winter until June. This cooling and its associated meridional SSTA  
363 gradient can drive meridional circulations. Its anomalous descending branch, located at  
364 about 20°N, can further depress the convection, suggesting reduced precipitation (Fig.  
365 9b) and cloud amount (Fig. 9c). In turn, cloud reduction can increase the surface  
366 shortwave radiation (Fig. 9d) and warm the sea surface. This feedback associated with  
367 circulation, precipitation, cloud and surface radiation could mitigate the SSTA cooling,  
368 leading to weakened meridional SST gradient in the late summer (shown in Fig.8d).

## 369 7. Conclusion and discussion

370 In this study, we investigated the changes in four precipitation extreme indices  
371 over China during the extended summer over 1961~2014. Observation analyses show  
372 that these four extreme indices have significantly increased over SEC and NWC whilst  
373 decreased over NEC and SWC. Based on a CMIP6 model HadGEM3-GC3.1 historical,  
374 GHG and AA simulations, we investigated the impacts of anthropogenic forcing  
375 (including GHG and AA forcings) on these observed trends over SEC and NWC. Our  
376 main results are summarized as follows.

- 377 1. Model reproduced the main features of increasing trends over SEC and NWC  
378 in historical simulation, suggesting a dominant role of forced changes in  
379 summer precipitation extremes over these two regions. Individual forcing  
380 simulations indicated that GHG and AA forcings have influences on summer  
381 extreme precipitation increases over SEC and NWC, respectively, through  
382 different processes.
- 383 2. Over SEC, extreme precipitation increase is primarily due to GHG forced  
384 increase in moisture flux convergence that is caused by both thermodynamic  
385 and dynamic effects. In response to GHG forcing, atmosphere can hold more  
386 moisture as temperature increases, which is favorable to precipitation increase.  
387 In addition, GHG forced El Nino-like SSTA pattern can weaken the Walker  
388 circulation, resulting in enhanced WNPSH and its associated anomalous  
389 southwesterlies, which transport more moisture to SEC and converge, giving

390 rise to local precipitation increase. Different from GHG effect, AA forced  
391 circulation anomalies favor more moisture flux convergence over SEC but that  
392 is offset by AA forced local evaporation reduction due to reduced downward  
393 shortwave radiation. Thus, net effect of AA forcing has a weak contribution to  
394 precipitation increase over SEC.

395 3. Over NWC, extreme precipitation increase is primarily attributed to AA forced  
396 moisture flux convergence increase and secondarily to GHG forced  
397 evaporation increase. Spatially heterogeneous AA emissions result in  
398 anomalous zonal temperature gradient and SLP gradient between NWC and  
399 north China. The SLPA gradient can drive warm and wet southwesterlies to  
400 turn northwestward after crossing the Huai River and converge over NWC,  
401 which favor local precipitation increase. In response to GHG forcing, clear sky  
402 downward longwave radiation increased over NWC, leading to local  
403 evaporation increase, which is favorable to precipitation increase.

404 Our results are generally in agreement with previous studies of anthropogenic  
405 impacts on East Asian precipitation changes based on CMIP5 models (Ma et al. 2017;  
406 Zhou et al. 2020). Although the observed increases in summer precipitation extremes  
407 over NWC have been captured by model, the underestimation of trends are prominent  
408 (blue bar in Fig. 2). It is recognized that model bias exists, however the reliability of  
409 observational dataset over NWC needs to be concerned. CN05.1 dataset is produced  
410 from more than 2400 stations covering mainland China, but stations available in  
411 western China are sparse, especially over the Taklimakan desert in NWC (Wu and Gao  
412 2013).

413 In addition, extreme precipitation changes over NEC and SWC have not further  
414 studied since model cannot reproduce the observed trends over these two regions in  
415 historical simulation. Simulation failure over SWC is possibly attributed to model bias  
416 due to complicated topography over there, which have been found to exist in many  
417 GCMs (Flato et al. 2013; Bao et al. 2015). While by comparison, the situation over  
418 NEC is different. From Fig.2 (blue bar) and Fig.3a-d, we found large inter-member  
419 spreads existing over NEC, which suggests that climate internal variability strongly  
420 influences, rather than external forcings, if perfect model is supposed. This issue  
421 whether summer extreme precipitation changes over NEC are dominated by internal  
422 variability deserves future investigation based on climate models with larger ensemble.

## 423 **Acknowledgements**

424 We acknowledge the international modeling groups for providing their data for  
425 analysis, the Program for Climate Model Diagnosis and Inter-comparison (PCMDI) for  
426 collecting and achieving the model data, the World Climate Research Programme's  
427 (WCRP's) Coupled Model Inter-comparison Project (CMIP) for organizing the model  
428 data analysis activity. This study is jointly supported by the National Key Research and  
429 Development Program of China (2020YFA0608201) and the NSFC project (41975078).  
430 BD is supported by the UK National Centre for Atmospheric Science, funded by the  
431 Natural Environment Research Council.

## 432 **Data Availability Statements**

433 The datasets generated and/or analyzed during the current study are available from  
434 the corresponding author on reasonable request.

## 435 **References**

- 436 Andrews, M. B., Ridley, J. K., Wood, R. A., Andrews, T., Blockley, E. W., Booth, B.,  
437 Burke, E., Dittus, A. J., Florek, P., Gray, L. J., Haddad, S., Hermanson, L., Hodson,  
438 D., Hogan, E., Jones, G. S., Knight, J. R., Kuhlbrodt, T., Misios, S., Mizielinski,  
439 M. S., Ringer, M. A., Robson, J., and Sutton, R. T. 2020: Historical simulations  
440 with HadGEM3-GC3.1 for CMIP6, *J. Adv. Model. Earth Syst.*,  
441 e2019MS001995, <https://doi.org/10.1029/2019MS001995>
- 442 Bao, J., J. Feng, and Y. Wang, 2015: Dynamical downscaling simulation and future  
443 projection of precipitation over China, *J. Geophys. Res. Atmos.*, 120, 8227–  
444 8243. Chen, H., and J. Sun, 2017: Contribution of human influence to increased  
445 daily precipitation extremes over China. *Geophys Res Lett*, 44, 2436-2444.
- 446 Collins, M., and Coauthors, 2010: The impact of global warming on the tropical Pacific  
447 Ocean and El Niño. *Nature Geoscience*, 3, 391-397.

448 Dong, B., L. J. Wilcox, E. J. Highwood, and R. T. Sutton, 2019: Impacts of recent  
449 decadal changes in Asian aerosols on the East Asian summer monsoon: roles of  
450 aerosol–radiation and aerosol–cloud interactions. *Clim Dyn*, 53, 3235-3256.

451 Dong, S., Y. Sun, and C. Li, 2020: Detection of human influence on precipitation  
452 extremes in Asia. *J. Climate*, 33, 5293–5304, [https://doi.org/10.1175/JCLI-D-19-](https://doi.org/10.1175/JCLI-D-19-0371.1)  
453 [0371.1](https://doi.org/10.1175/JCLI-D-19-0371.1).

454 Dong S, Sun Y, Li C, Zhang X, Min S, Kim Y (2021) Attribution of extreme  
455 precipitation with updated observations and CMIP6 simulations. *J Clim*  
456 34(3):871–881. <https://doi.org/10.1175/jcli-d-19-1017.1>

457 Eyring V, Bony S, Meehl GA, Senior CA, Stevens B, Stoufer RJ, Taylor KE (2016)  
458 Overview of the coupled model intercomparison project phase 6 (CMIP6)  
459 experimental design and organization. *Geosci Model Dev* 9:1937–1958.  
460 <https://doi.org/10.5194/gmd-9-1937-2016>

461 Flato, G., et al. (2013), Evaluation of climate models, in *Climate Change 2013: The*  
462 *Physical Science Basis. Contribution of Working Group I to the Fifth*  
463 *Assessment Report of the Intergovernmental Panel on Climate Change,*  
464 *Cambridge Univ. Press, Cambridge, U. K., and New York.*

465 Gillett NP, Shiogama H, Funke B et al (2016) The detection and attribution model  
466 intercomparison project (DAMIP v1.0) contribution to CMIP6. *Geosci Model Dev*  
467 9:3685–3697

468 IPCC, 2021: *Climate Change 2021: The Physical Science Basis. Contribution of*  
469 *Working Group I to the Sixth Assessment Report of the Intergovernmental Panel*  
470 *on Climate Change. Cambridge University Press, Cambridge, UK and New York,*  
471 *NY, USA, in press.*

472 Lau, K. M., and H. T. Wu, 2007: Detecting trends in tropical rainfall characteristics,

473 1979–2003. *Int. J. Climatol.*, **27**, 979–988.

474 Li, H., H. Chen, and H. Wang, 2017: Effects of anthropogenic activity emerging as  
475 intensified extreme precipitation over China. *Journal of Geophysical Research:*  
476 *Atmospheres*, 122, 6899-6914.

477 Li, X., M. Ting, C. Li, and N. Henderson, 2015: Mechanisms of Asian Summer  
478 Monsoon Changes in Response to Anthropogenic Forcing in CMIP5 Models %J  
479 *Journal of Climate*. *J Climate*, 28, 4107-4125.

480 Lin, L., Y. Xu, Z. Wang, C. Diao, W. Dong, and S.-P. Xie, 2018: Changes in Extreme  
481 Rainfall Over India and China Attributed to Regional Aerosol-Cloud Interaction  
482 During the Late 20th Century Rapid Industrialization. *Geophys Res Lett*, 45, 7857-  
483 7865.

484 Lin, Z., B. Dong, and Z. Wen, 2020: The effects of anthropogenic greenhouse gases and  
485 aerosols on the inter-decadal change of the South China Sea summer monsoon in  
486 the late twentieth century. *Clim Dyn*, 54, 3339-3354.

487 Lu, C., F. C. Lott, Y. Sun, P. A. Stott, and N. Christidis, 2020: Detectable Anthropogenic  
488 Influence on Changes in Summer Precipitation in China, *J Climate*, 33, 5357-5369.

489 Luo, F., B. Dong, F. Tian, and S. Li, 2019: Anthropogenically Forced Decadal Change  
490 of South Asian Summer Monsoon Across the Mid-1990s. *Journal of Geophysical*  
491 *Research: Atmospheres*, 124, 806-824.

492 Luo, N., Y. Guo, J. Chou, and Z. Gao: Added value of CMIP6 models over CMIP5  
493 models in simulating the climatological precipitation extremes in China,  
494 *International Journal of Climatology*, 1-17, doi:10.1002/joc.7294.

495 Ma, S., and Coauthors, 2017: Detectable Anthropogenic Shift toward Heavy  
496 Precipitation over Eastern China. *J Climate*, 30, 1381-1396.

497 Min, S.-K., X. Zhang, F. W. Zwiers, and G. C. Hegerl, 2011: Human contribution to

498 more-intense precipitation extremes. *Nature*, 470, 378-381.

499 Peng, D., and T. Zhou, 2017: Why was the arid and semiarid northwest China getting  
500 wetter in the recent decades? *Journal of Geophysical Research: Atmospheres*, 122,  
501 9060-9075.

502 Qin DH, Zhang JY, Shan CC, Song LC. 2015. China National Assessment Report on  
503 Risk Management and Adaptation of Climate Extremes and Disasters (Refined  
504 Edition). Science Press: Beijing, 124 pp.

505 Song, F., T. Zhou, and Y. Qian, 2014: Responses of East Asian summer monsoon to  
506 natural and anthropogenic forcings in the 17 latest CMIP5 models. *Geophys Res*  
507 *Lett*, 41, 596-603.

508 Sun, Y., S. Dong, T. Hu, X. Zhang, and P. Stott, 2019: Anthropogenic Influence on the  
509 Heaviest June Precipitation in Southeastern China since 1961, *B Am Meteorol Soc*,  
510 100, S79-S83.

511 Tian, F., B. Dong, J. Robson, and R. Sutton, 2018: Forced decadal changes in the East  
512 Asian summer monsoon: the roles of greenhouse gases and anthropogenic aerosols.  
513 *Clim Dyn*, 51, 3699-3715.

514 Trenberth, K. E., and C. J. Guillemot, 1995: Evaluation of the Global Atmospheric  
515 Moisture Budget as Seen from Analyses, *J Climate*, 8, 2255-2272.

516 Trenberth, K. E., A. Dai, R. M. Rasmussen, and D. B. Parsons, 2003: The changing  
517 character of precipitation. *Bull. Amer. Meteor. Soc.*, **84**, 1205–1218.

518 Wu, J., and X.-J. Gao, 2013: A gridded daily observation dataset over China region and  
519 comparison with the other datasets, *Chinese J Geophysics*, 56, 1102-1111 (in  
520 Chinese).

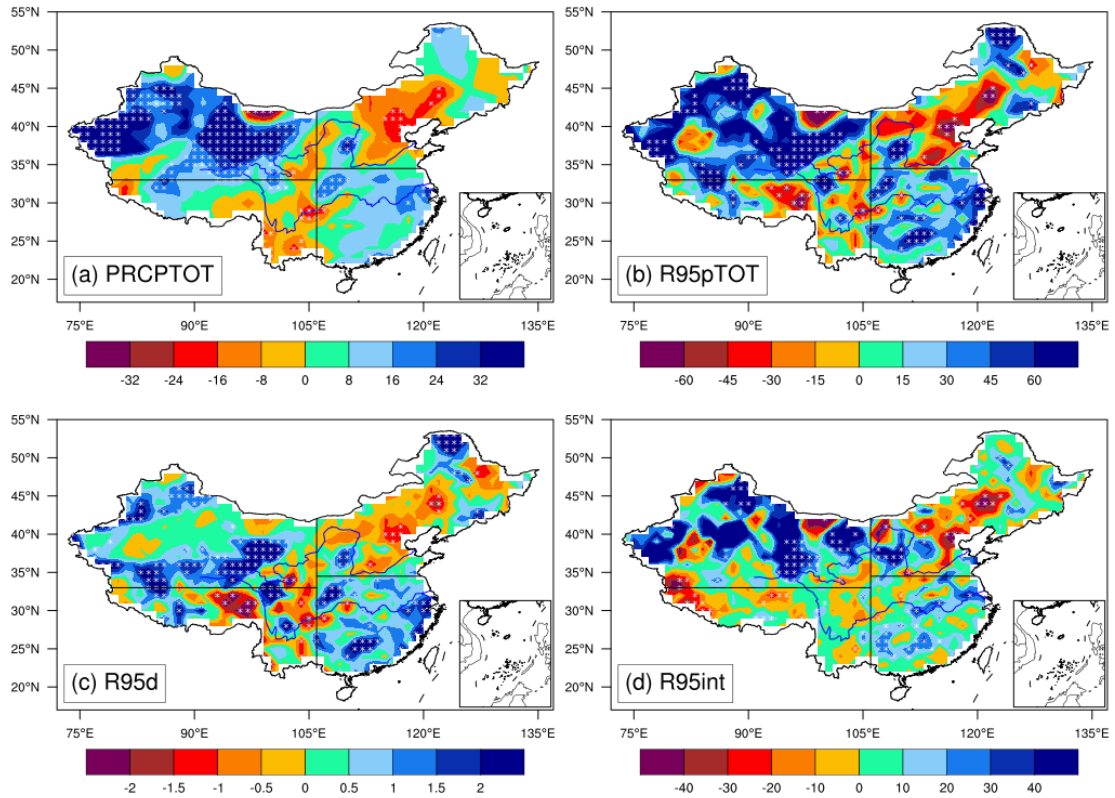
521 Zhang, L., P. Wu, and T. Zhou, 2017: Aerosol forcing of extreme summer drought over  
522 North China. *Environmental Research Letters*, 12, 034020.

523 Zhang, X., H. Wan, F. W. Zwiers, G. C. Hegerl, and S.-K. Min, 2013: Attributing  
524 intensification of precipitation extremes to human influence, *Geophys Res Lett*,  
525 40, 5252-5257.

526 Zhou, B., Y. Xu, J. Wu, S. Dong, and Y. Shi, 2016: Changes in temperature and  
527 precipitation extreme indices over China: analysis of a high-resolution grid dataset,  
528 *International Journal of Climatology*, 36, 1051-1066.

529 Zhou T, W Zhang, et al., 2020: The dynamic and thermodynamic processes dominating  
530 the reduction of global land monsoon precipitation driven by anthropogenic  
531 aerosols emission, *Science China (Earth Sciences)*, 63, 919-933.

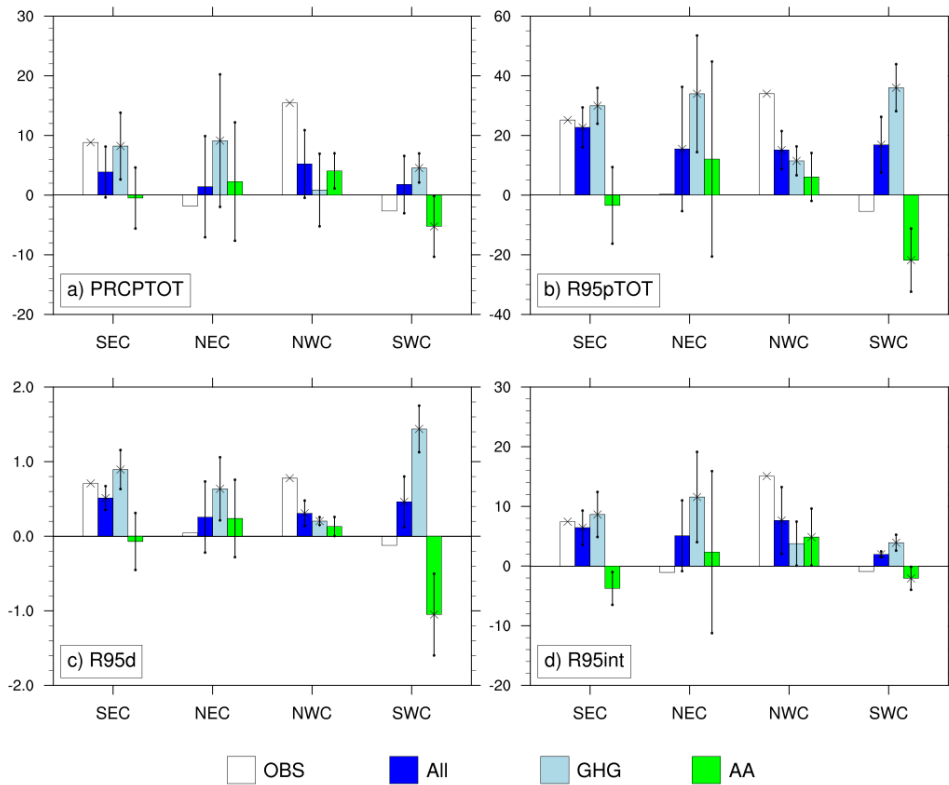
532



533

534 FIG.1 Observed linear trends in summer precipitation extremes during 1961~2014 (54  
 535 years as 54a): (a) PRCPTOT (%/54a), (b) R95pTOT (%/54a), (c) R95d (days/54a) and  
 536 (d) R95int (%/54a). Changes in PRCPTOT, R95pTOT, and R95int are expressed as  
 537 percentage relative to the climatologic mean over 1961~1990. The cross marks denote  
 538 trends being statistically significant at the 90% confidence level using two-tailed  
 539 Student's t-test. The straight lines divide China into southeast China (SEC), northeast  
 540 China (NEC), northwest China (NWC) and southwest China (SWC) which are used for  
 541 regional mean analysis.

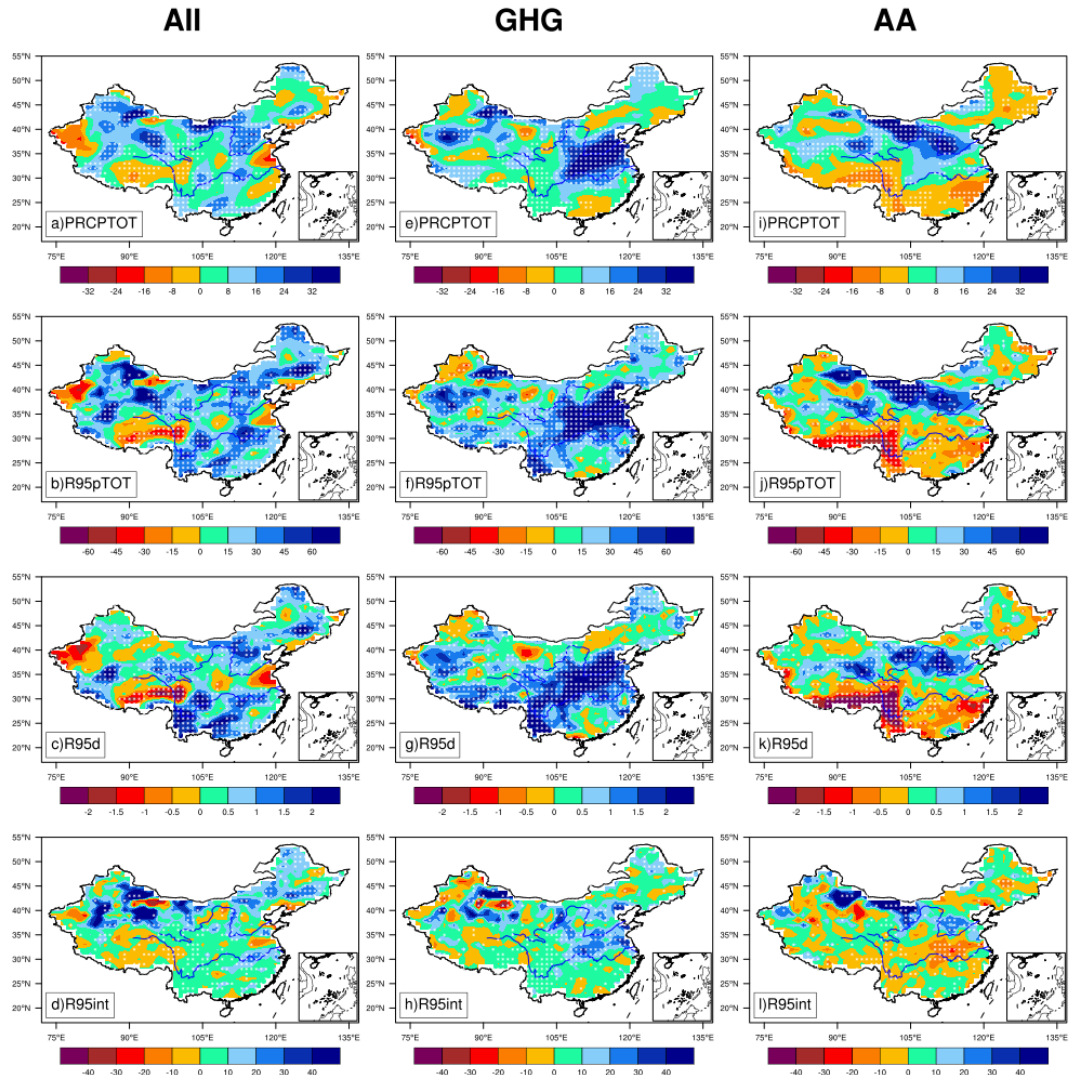
542



543

544 FIG. 2 Observed and model simulated linear trends of regional averaged summer  
 545 precipitation extremes during 1961~2014 in response to All forcing, GHG forcing and  
 546 AA forcing over southeast China (SEC), northeast China (NEC), northwest China  
 547 (NWC) and southwest China (SWC) (Fig. 1). Changes in PRCPTOT, R95pTOT, and  
 548 R95int are expressed as percentage relative to the climatologic mean over 1961~1990  
 549 with units of %/54a; unit for R95d is days/54a. The bars are ensemble mean; the dots  
 550 are ensemble mean  $\pm$  one standard deviation across five ensemble members; the cross  
 551 marks denote trends being statistically significant at the 90% confidence level using  
 552 two-tailed Student's t-test.

553

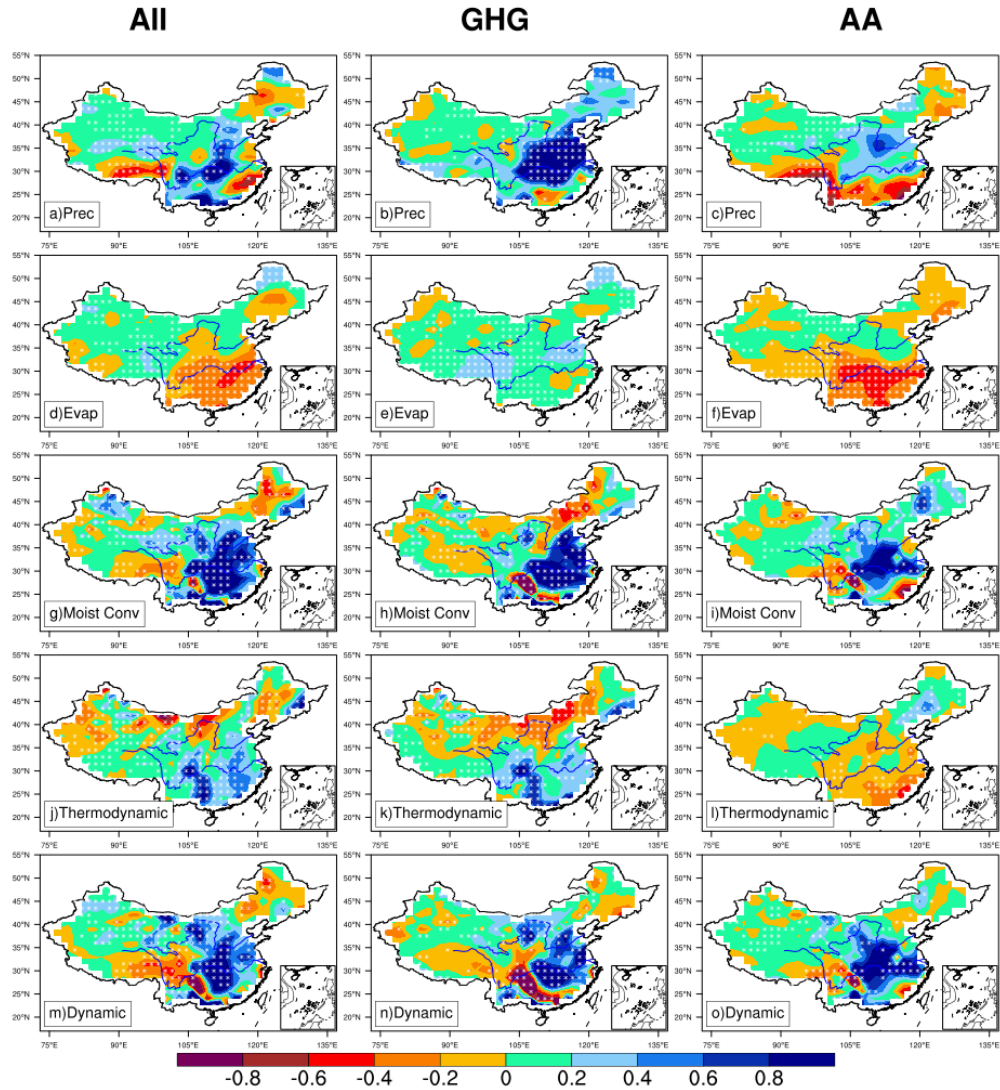


554

555 FIG. 3 Model simulated linear trends in summer PRCPTOT (%/54a), R95pTOT  
 556 (%/54a), R95d (days/54a), and R95int (%/54a) during 1961~2014 in response to (a-d)  
 557 All forcing, (e-h) GHG forcing, and (i-l) AA forcing. Changes in PRCPTOT, R95pTOT,  
 558 and R95int are expressed as percentage relative to the climatologic mean over  
 559 1961~1990. The shadings are ensemble mean; the cross marks denote signal-to-noise  
 560 ratio larger than 1 (signal: ensemble mean; noise: one standard deviation across five  
 561 ensemble members).

562

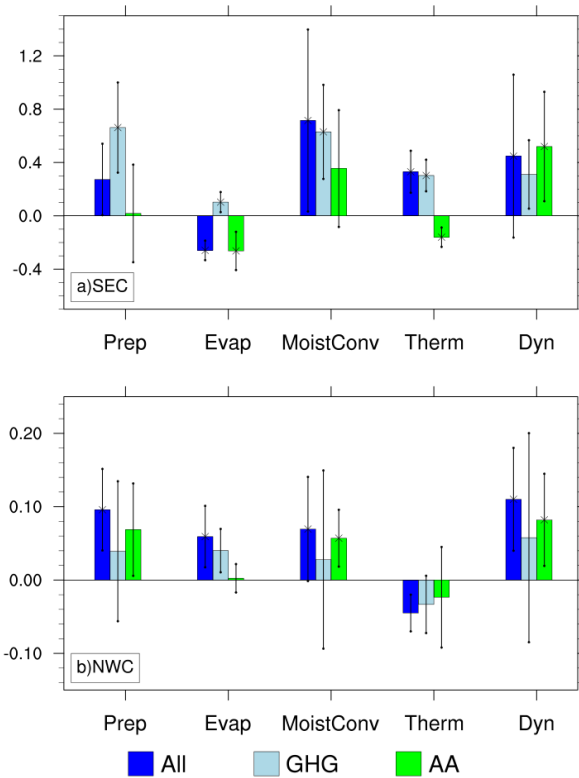
563



564  
 565 FIG.4 Model simulated linear trends in summer (a-c) total precipitation ( $\text{mm day}^{-1}/54\text{a}$ ),  
 566 (d-f) evaporation ( $\text{mm day}^{-1}/54\text{a}$ ), (g-i) moisture flux convergence ( $\text{mm day}^{-1}/54\text{a}$ ), (j-  
 567 k) thermodynamic component ( $\text{mm day}^{-1}/54\text{a}$ ), and (m-o) dynamic component ( $\text{mm}$   
 568  $\text{day}^{-1}/54\text{a}$ ) during 1961~2014 in response to All forcing, GHG forcing and AA forcing.  
 569 The shadings are ensemble mean; the cross marks denote the signal-to-noise ratio larger  
 570 than 1 (signal: ensemble mean; noise: one standard deviation across five ensemble  
 571 members).

572

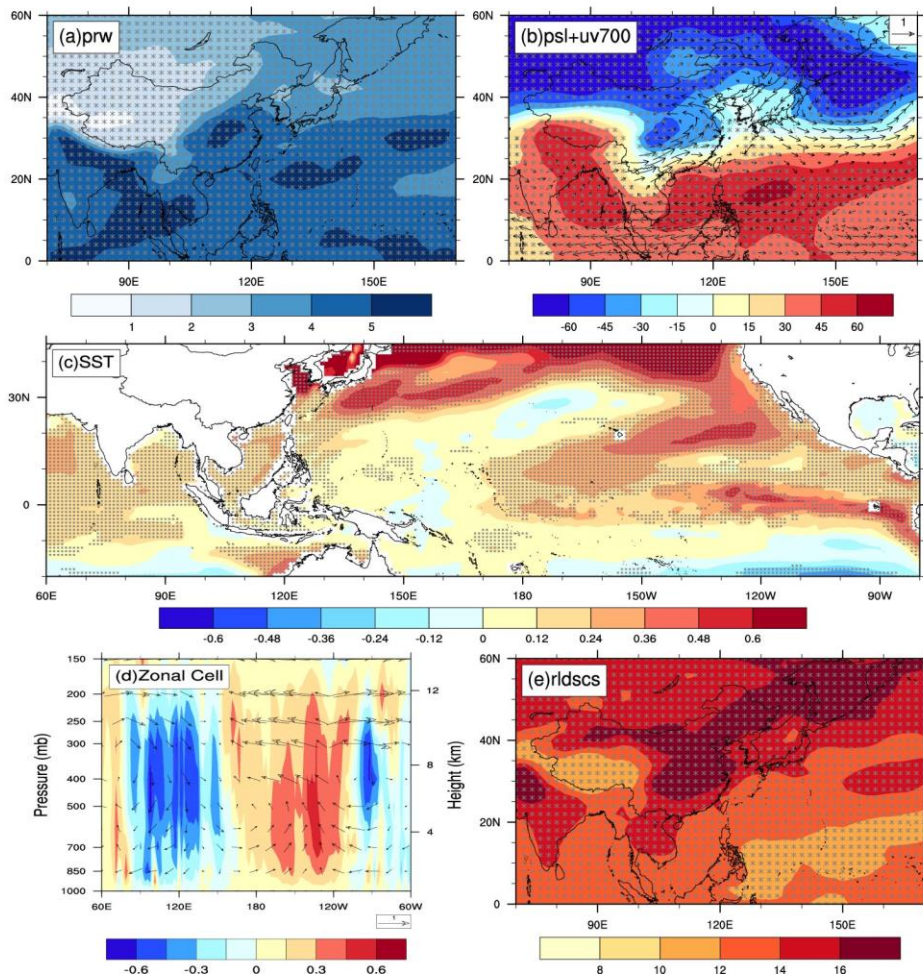
573



574

575 FIG.5 Model simulated linear trends in regional averaged summer precipitation (mm  
 576 day<sup>-1</sup>/54a), evaporation (mm day<sup>-1</sup>/54a), moisture flux convergence (mm day<sup>-1</sup>/54a),  
 577 thermodynamic component (mm day<sup>-1</sup>/54a) and dynamic component (mm day<sup>-1</sup>/54a)  
 578 during 1961~2014 in response to All forcing, GHG forcing and AA forcing over (a)  
 579 southeast China and (b) northwest China. The bars are ensemble mean; the dots are  
 580 ensemble mean±one standard deviation across five ensemble members; the cross marks  
 581 denote trends being statistically significant at the 90% confidence level using two-tailed  
 582 Student's t-test.

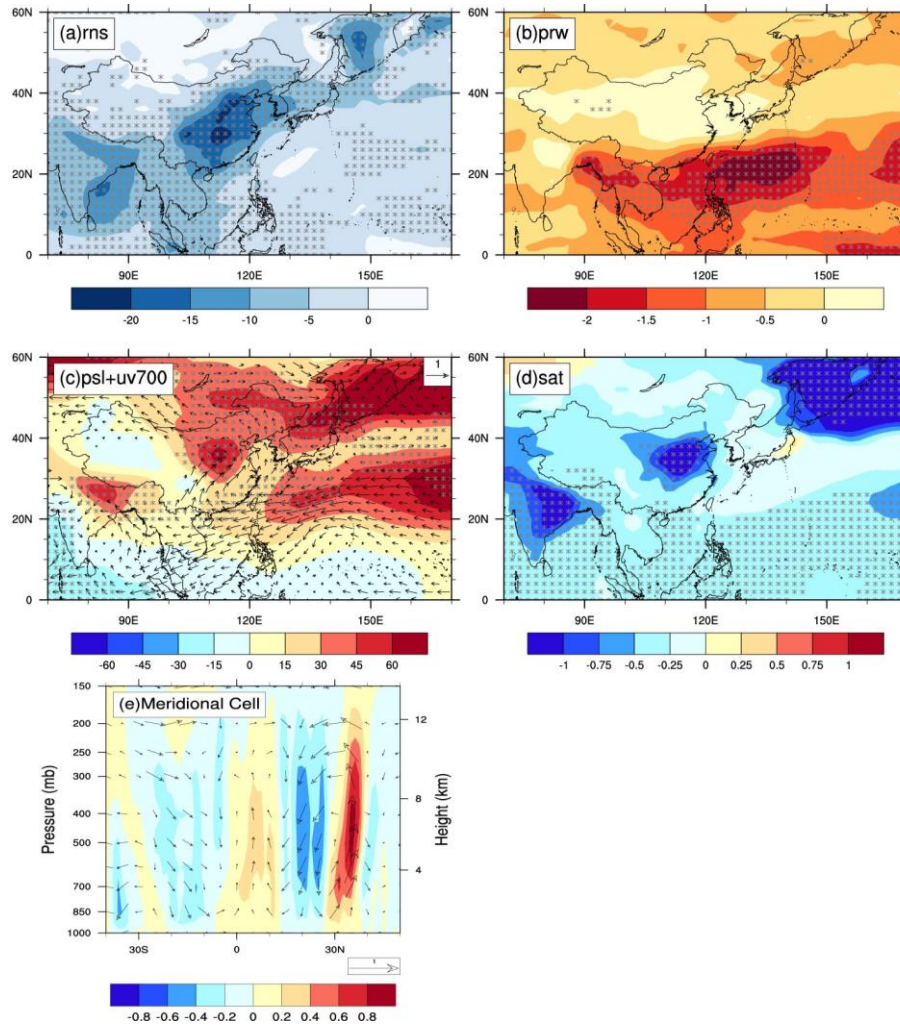
583



584

585 FIG.6 Model simulated (ensemble mean) linear trends during summer in response to  
 586 GHG forcing. (a) Precipitable water ( $\text{Kg m}^{-2}/54\text{a}$ ), (b) sea level pressure (shadings,  
 587  $\text{Pa}/54\text{a}$ ) and 700hPa horizontal winds (vectors,  $\text{m s}^{-1}/54\text{a}$ ), (c) sea surface temperature  
 588 ( $^{\circ}\text{C}/54\text{a}$ ), (d) omega (shadings,  $\text{Pa s}^{-1}/54\text{a}$ ) and omega-u vectors averaged over  $5^{\circ}\text{S}\sim 20^{\circ}$   
 589 N and (e) clear sky surface downward longwave radiation ( $\text{W m}^{-2}/54\text{a}$ ). Omega is scaled  
 590 to match the value of meridional wind and its sign is reversed. The cross marks denote  
 591 the signal-to-noise ratio larger than 1 (signal: ensemble mean; noise: one standard  
 592 deviation across five ensemble members).

593

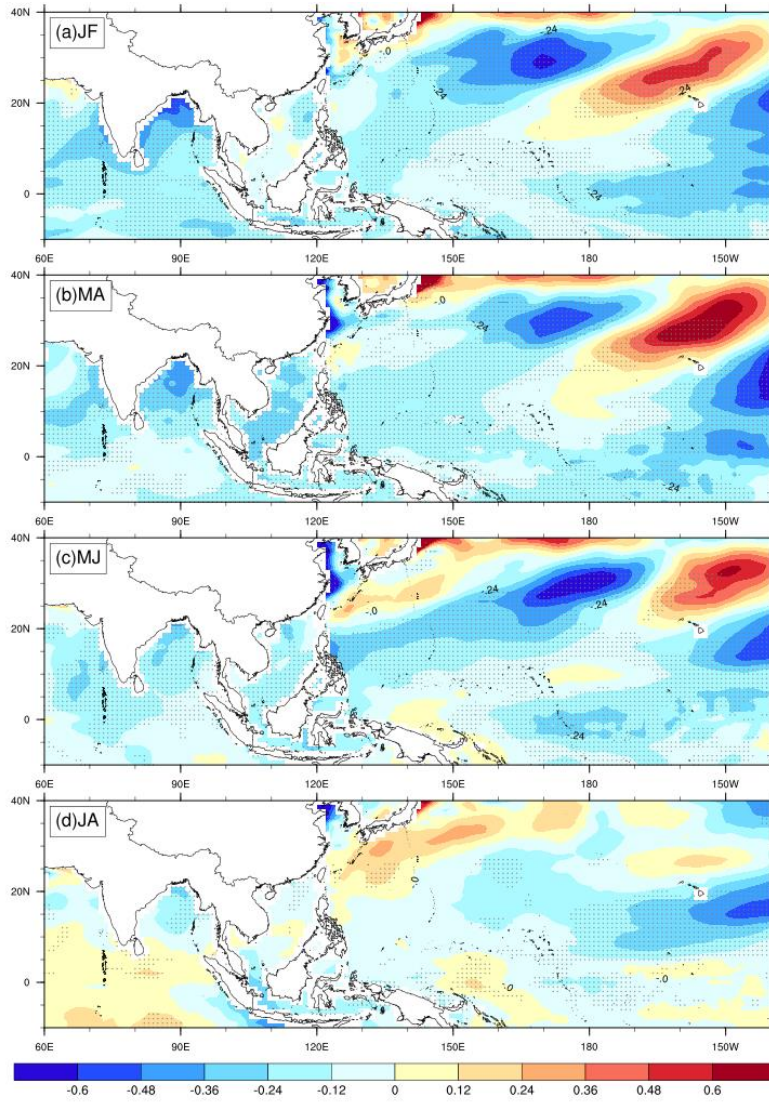


594

595 FIG.7 Model simulated (ensemble mean) linear trends during summer in response to  
 596 AA forcing. (a) Net surface radiation ( $\text{W m}^{-2}/54\text{a}$ ), (b) precipitable water ( $\text{Kg m}^{-2}/54\text{a}$ ),  
 597 (c) sea level pressure (shadings,  $\text{Pa}/54\text{a}$ ) and 700hPa horizontal winds (vectors,  $\text{m s}^{-1}/54\text{a}$ ), (d)  
 598 near-surface air temperature ( $\text{K}/54\text{a}$ ) and (e) omega (shadings,  $\text{Pa s}^{-1}/54\text{a}$ )  
 599 and omega-v vectors averaged over  $105^{\circ}\text{E} \sim 145^{\circ}\text{E}$ . Omega is scaled to match the value  
 600 of meridional wind and its sign is reversed. The cross marks denote the signal-to-noise  
 601 ratio larger than 1 (signal: ensemble mean; noise: one standard deviation across five  
 602 ensemble members).

603

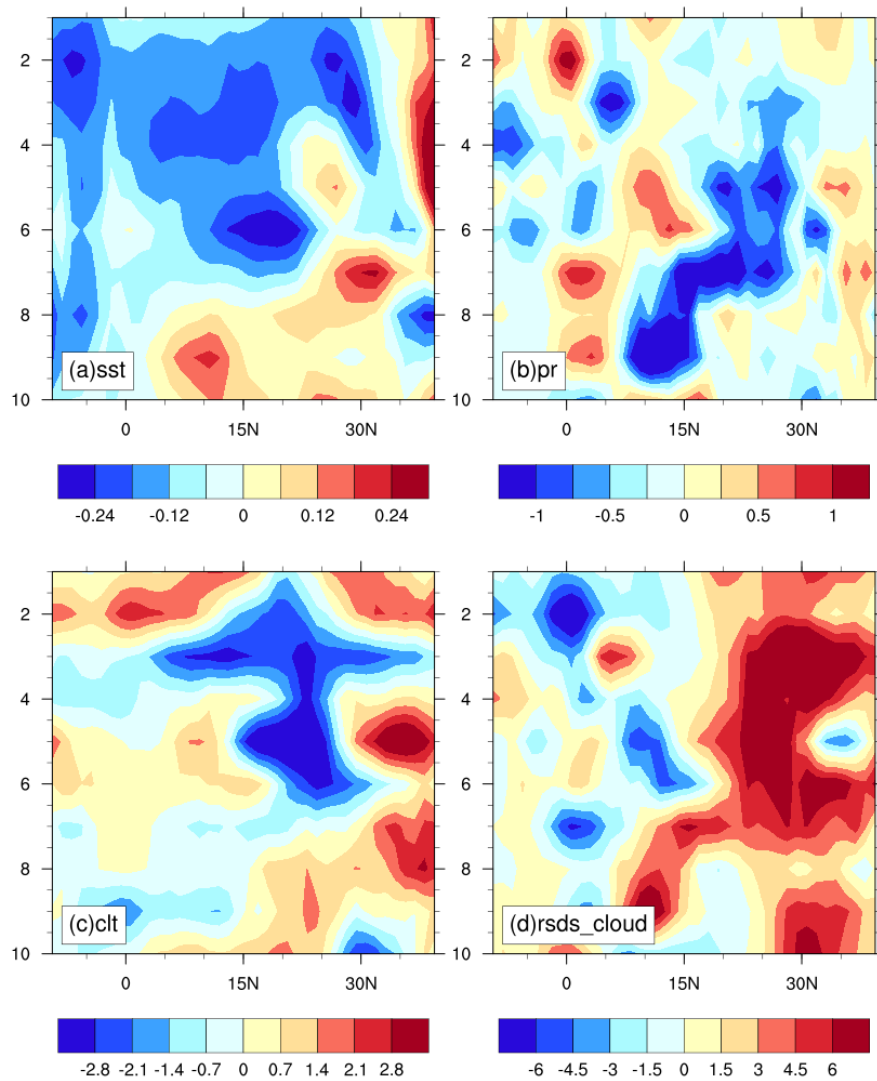
604



605

606 FIG. 8 Model simulated (ensemble mean) linear trends in sea surface temperature  
 607 (°C/54a) in response to AA forcing from preceding winter to summer. The cross marks  
 608 denote the signal-to-noise ratio larger than 1 (signal: ensemble mean; noise: one  
 609 standard deviation across five ensemble members).

610



611

612 FIG.9 Evolution of model simulated (ensemble mean) linear trends averaged over 105°

613 E ~145°E from January to October in response to AA. (a) Sea surface temperature

614 (°C/54a), (b) precipitation (mm day<sup>-1</sup>/54a), (c) total cloud amount (%/54a) and (d)

615 surface downward shortwave radiation related with cloud (W m<sup>-2</sup>/54a).

616

617